Materials Science & Engineering A 924 (2025) 147819

Contents lists available at ScienceDirect

Materials Science & Engineering A

journal homepage: www.elsevier.com/locate/msea

Unusual low-temperature ductility increase mediated by dislocations alone

Muhammad Naeem [a,b,1], Yuemin Ma [a,j,1], Jin Tian [c,1], Haojie Kong [d], Liliana Romero-Resendiz [b,e,f], Ziyang Fan [a,g], Feng Jiang [c], Wu Gong [h], Stefanus Harjo [h], Zhaoxuan Wu [i,*], Xun-Li Wang [a,j,**]

[a] Department of Physics and Center for Neutron Scattering, City University of Hong Kong, Kowloon, Hong Kong
[b] School of Metallurgy and Materials, University of Birmingham, Birmingham, B15 2TT, UK
[c] State Key Laboratory for Mechanical Behavior of Materials, Xi'an Jiaotong University, Xi'an, 710049, China
[d] School of Materials Science and Engineering, Dongguan University of Technology, Dongguan, 523808, China
[e] Facultad de Química, Departamento de Ingeniería Metalúrgica, Universidad Nacional Autónoma de México, Mexico City, 04510, Mexico
[f] Department of Design and Engineering, Faculty of Science and Technology, Bournemouth University, Poole, Dorset, BH12 5BB, UK
[g] City University of Hong Kong (Dongguan), Dongguan, 523000, China
[h] J-PARC Center, Japan Atomic Energy Agency, Tokai, Ibaraki, 319-1195, Japan
[i] Department of Materials Science and Engineering, City University of Hong Kong, Kowloon, Hong Kong
[j] Shenzhen Research Institute of City University of Hong Kong, Shenzhen Hi-Tech Industrial Park, Shenzhen, 518057, China

ARTICLE INFO

Keywords:
Multi-principal element alloy
Cryogenic deformation
In situ testing
Dislocation-mediated plasticity
Dislocation dynamics

ABSTRACT

Face-centered cubic (fcc) medium- and high-entropy alloys (M/HEAs) are known to exhibit enhanced strength−ductility combination at cryogenic temperatures. These superior mechanical properties have been commonly associated with the activation of additional deformation mechanisms such as stacking faults, twinning, and/or martensitic phase transformation. Here, using *in situ* tensile testing with neutron diffraction, we present experimental evidence of an enhanced strain hardening in VCoNi MEA, mediated solely by dislocations instead. At 15 K, VCoNi MEA shows increased yield strength, strain hardening, and fracture strain. Analysis of the *in situ* neutron diffraction data demonstrates that the strain hardening in this alloy is driven by faster dislocation accumulation, without the formation of stacking/twin faults or martensite. This low-temperature behavior can be rationalized by considering the Orowan equation and challenges the conventional wisdom on strength−ductility enhancement at cryogenic temperatures in fcc M/HEAs. Our study sheds light on the influence of dislocation mobility on plastic behaviors and highlights the importance of dislocation-mediated plasticity at low temperatures.

1. Introduction

Multi-principal element medium- and high-entropy alloys (M/HEAs) have complex atomic heterogeneity and severe lattice distortion, which are the key properties endowing them with excellent resistance to corrosion and irradiation, enhanced hardness, high lattice friction, and dislocation core-associated behavior [1–5]. Among them, face-centered cubic (fcc) M/HEAs possess atypical high strength and high ductility simultaneously, in contrast to the inverse strength−ductility relationship in most conventional alloys. One notable example is the equiatomic CrCoNi, a ternary MEA with a strength−ductility combination better than the quaternary CrFeCoNi and quinary CrMnFeCoNi fcc HEAs [6–8]. A recent addition to this realm is VCoNi, which has severe lattice distortion due to the incorporation of vanadium with a large misfit volume. At a grain size of 5.6 μm, VCoNi exhibits an exceptional yield strength of 767 MPa at room temperature (RT), far better than those of CrCoNi with a comparable grain size [9].

At cryogenic temperatures, fcc M/HEAs further exhibit preferable mechanical behavior absent in many conventional alloys. Specifically, their strength, ductility and toughness increase with decreasing temperature [6,10–14], defying many extant studies on conventional metals and alloys. This superior property combination has been attributed to

* Corresponding author. Department of Materials Science and Engineering, City University of Hong Kong, Kowloon, Hong Kong.
** Corresponding author. Department of Physics and Center for Neutron Scattering, City University of Hong Kong, Kowloon, Hong Kong.
E-mail addresses: zhaoxuwu@cityu.edu.hk (Z. Wu), xlwang@cityu.edu.hk (X.-L. Wang).
[1] These authors contributed equally.

https://doi.org/10.1016/j.msea.2025.147819
Received 7 November 2024; Received in revised form 5 January 2025; Accepted 6 January 2025
Available online 7 January 2025

the activation of additional deformation mechanisms at lower temperatures [6,8,10,15,16]. For the prototypic fcc CrMnFeCoNi Cantor alloy, plastic deformation is carried out by dislocation glide, all the way up to fracture at RT [17]. At low temperatures, multiple deformation mechanisms are activated, including deformation twinning, formation of stacking faults (SFs) and martensitic phase transformations [6–8, 10–16]. These different mechanisms have disparate transition paths and are activated heterogeneously at local stress concentrations or composition-favorable sites. Their operations not only provide progressive stress relieving and energy dissipation, but also create planar faults acting as barriers to dislocations on other slip planes, resulting in twinning-induced plasticity (TWIP) and transformation-induced plasticity (TRIP) effects seen in some austenitic steels [18]. These additional mechanisms are thus believed to lead to microstructure refinement and effective strain hardening, which in turn delays plastic instability such as necking/shear localization and enables more uniform tensile elongation at cryogenic temperatures. This apparent deformation mechanism−property proposition is further substantiated by theoretical studies where (i) density functional theory (DFT) calculations show that the stacking fault energy (SFE) decreases with reducing temperature in the Cantor alloy [19], and (ii) established models predict that lower SFE favors twinning and fcc-to-hcp (hexagonal close-packed) martensitic phase transformation [20,21]. However, VCoNi MEA also exhibits enhanced strength−ductility at lower temperatures, even down to 4.2 K [22], but purportedly without the activation of additional deformation mechanisms, or the TWIP/TRIP effects. The post-mortem TEM study shows that the deformation features are largely similar in VCoNi deformed at RT and 4.2 K [22]. In fact, many other fcc elemental metals (e.g., Al, Cu, Ag), solid solution and precipitate-strengthened alloys exhibit similar strength−ductility enhancement with decreasing temperature [10,13,23–25]. These experimental observations suggest a common deformation mechanism responsible for the improved mechanical properties in fcc systems at low temperatures. Up to date, however, the physical mechanisms underlying this unconventional low-temperature deformation behavior have remained elusive.

In this work, we studied the tensile deformation of VCoNi MEA at both RT and an ultralow temperature of 15 K. VCoNi provides an excellent example to highlight, as other deformation mechanisms (SF formation, deformation twinning and martensitic phase transformation) are not activated at these test temperatures. DFT calculations also show that VCoNi with chemical short range ordering (SRO) has a high SFE (226 ± 81 mJ/m^2) and a twinnability lower than all elemental fcc metals [20]. Our *in situ* neutron diffraction experiments reveal critical deformation characteristics and mechanisms, including lattice strain, texture and dislocation density evolutions throughout the entire deformation process. Quantitative analysis of these experimental data demonstrates that the deformation behaviors at RT and 15 K are essentially the same, though with different stresses and ductilities. At both temperatures, two regimes of dislocation accumulation are observed and the strain hardening rates follow the dislocation density evolution. At 15 K, the enhanced strength−ductility is enabled by higher strain-hardening rate driven by an earlier switch to the faster dislocation accumulation regime and a high dislocation density necessitated by the reduced mean free path of dislocations. The switch of the two-stage regime may correspond to a change from single-slip dominated to multi-slip dominated plastic deformation.

2. Material and methods

2.1. Sample preparation

The equiatomic VCoNi alloys were produced by arc melting of pure elements (purity >99.9 wt %). The melt was cast into Cu mold with dimensions of 10 mm × 40 mm × 60 mm. The slabs obtained in this way were homogenized at 1373 K for 1 h and then water quenched. This was followed by hot rolling at 1273 K to achieve around 40 % reduction in thickness. The hot rolled samples were annealed at 1373 K for 30 min and water quenched again. The samples were then cold rolled with a thickness reduction of ~65 %. Finally, recrystallization was carried out in air at 1373 K for 30 min, followed by water quenching. The average grain size was ~30 μm after the above thermo-mechanical processing steps. Uniaxial tensile test specimens were cut via electric discharge machining into flat dog bone shape and with gauge dimensions of 25 mm × 4 mm × 3 mm (length × width × thickness).

2.2. In situ neutron diffraction measurements

Uniaxial tensile loadings were carried out in conjunction with *in situ* neutron diffraction measurements at the TAKUMI Engineering Materials beamline, Materials and Life Science Experimental Facility at the Japan Proton Accelerator Research Complex (J-PARC). The experiments at 15 K were conducted using a cryogenic load cell coupled with a GM cooler. The cryogenic loading chamber was evacuated below 10^{-4} Pa. The samples were cooled down and held at 15 K before loading. The change in lattice parameter during cooling is given in Fig. 1, together with that of CrCoNi and CrFeCoNi for comparisons. It can be seen that VCoNi displays the lowest coefficient of thermal expansion. To acquire the neutron diffraction data during loading, two detector banks were used at ±90° to the incident beam for recording information along the loading direction (LD) and transverse direction (TD) simultaneously. Tensile tests were performed at a strain rate of 2.67×10^{-5} s^{-1} with real-time observations to investigate the deformation behavior and characteristics at RT (293 K) and 15 K.

2.3. Microstructure characterization

The microstructure of samples was characterized by means of electron backscatter diffraction (EBSD) using a JEOL-7800F field-emission gun scanning electron microscope equipped with a Nordlys Max3 EBSD detector. The data analysis was performed in the Channel 5 software package. A step size of 0.075 μm was used for all the scanning maps. The selected surface perpendicular to the loading direction was ground and polished using alumina suspension of 0.5 μm particle size. An additional electropolishing was performed using a solution of 85 vol.% ethyl alcohol, 10 vol.% 2-Butoxy ethanol and 5 vol.% perchloric acid at 15 °C with a voltage of 35 V. The transmission electron microscope (TEM) observation was conducted by JEOL JEM-2100F with samples welded on copper grids. TEM samples were prepared by mechanically grinding

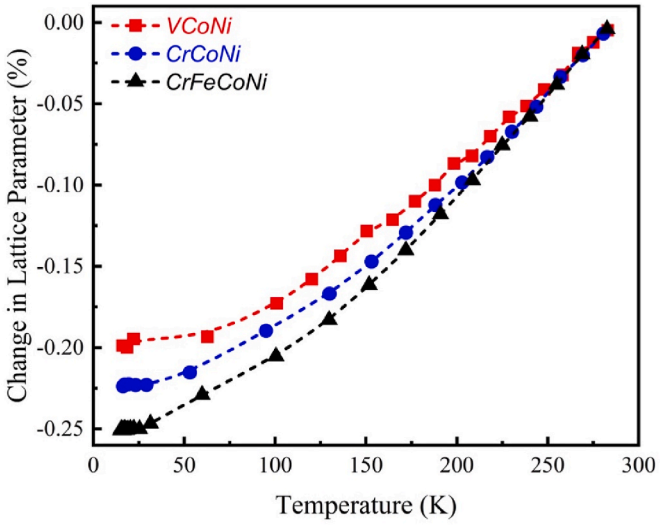

Fig. 1. Change in lattice parameter upon cooling. The comparison of VCoNi, CrCoNi, and CrFeCoNi alloys upon cooling from room temperature to 15 K shows the lowest coefficient of thermal expansion for the VCoNi alloy.

the bulk samples to obtain a thin foil of 50 μm. The sample foil was punched into a disc of 3 mm diameter. A dimple grinder (Gatan Dimple Grinder II) was used to further thin the disc to 10 μm. Ion milling was performed by directing an Ar^{+} ion beam at 3 kV using a precision ion polishing system (Gatan PIPS II 695) until the disc reached electron transparency for TEM observations.

3. Results

3.1. Enhancement of mechanical properties at cryogenic temperature

Fig. 2a shows the respective engineering stress-strain curves. Table 1 lists measured mechanical properties at RT and 15 K. Despite a relatively coarse average grain size of ~30 μm, the alloy possesses a relatively high yield strength (σ_y) of 438 MPa, an ultimate tensile strength (σ_u) of 949 MPa, and a strain to fracture (ε_f) of 61 % at RT. At 15 K, all these mechanical properties are enhanced, with σ_y, σ_u and ε_f increased to 746 MPa, 1325 MPa and 73 %, respectively. Fig. 2b depicts the evolution of strain-hardening rates superimposed on the true stress-true strain curves. The sample at 15 K exhibits a high strain-hardening rate $\frac{d\sigma}{d\varepsilon}$ of ~2600 MPa in the early-stage plastic deformation. The hardening rate increases moderately (~10 %) during subsequent straining up to a true strain of 0.4 and the onset of necking. In the strain range of $0.05 < \varepsilon < 0.4$, plastic deformation resembles Stage II deformation with nearly constant $\frac{d\sigma}{d\varepsilon}$ in many conventional metals and alloys. The plastic flow and hardening behavior are also similar to that of other fcc M/HEAs at cryogenic temperatures [8,11,13,26]. In contrast, the strain-hardening rate at RT is lower throughout the entire deformation process; the hardening rate starts at ~2000 MPa during early-stage plastic deformation, maintains a nearly-constant rate for an extended strain range $0.1 < \varepsilon < 0.35$ typical of Stage II deformation (forest hardening), and gradually decreases until fracture.

3.2. Similar lattice strain and texture evolution at room and cryogenic temperatures

Table 2 shows the elastic moduli E_{hkl} along specific crystallographic orientations. The E_{hkl} values were obtained from a linear fit to the lattice strain ε_{hkl} along the loading direction (LD) in the *elastic* region. Here, the lattice strain perpendicular to the specific {*hkl*} plane is given by: $\varepsilon_{hkl} = \frac{d_{hkl} - d^0_{hkl}}{d^0_{hkl}}$, where d_{hkl} and d^0_{hkl} are the interplanar spacing for the {*hkl*} plane during deformation and before deformation, respectively. The ⟨111⟩ direction is the stiffest and ε_{111} the smallest, while ⟨100⟩ is the most compliant direction in the elastic region. All elastic moduli E_{hkl} increase at 15 K, i.e., the fcc lattice becomes stiffer with decreasing temperature, as in other M/HEAs [13,26–28] (this is a universal behavior with the exception of Elinvar alloys [29]). Furthermore, the elastic anisotropy, as measured by E_{111}/E_{200}, decreases slightly at 15 K, again similar to that of other M/HEAs [13,26–28]. The macroscopic elastic modulus of alloy (E_{fcc}), as obtained from the linear fitting of the lattice parameter a as a function of uniaxial loading σ in the elastic region, also shows a moderate increase with decreasing temperature (Table 2), which is consistent with the Young's moduli obtained from the stress-strain curves (Table 1).

Fig. 3a and b shows the evolution of lattice strains ε_{hkl} at RT and 15 K oriented along the LD. Lattice strain is a measure of elastic deformation/stress in different families of grains, arising from the intergranular strains. For grains of different orientations (relative to the LD), different lattice strains develop due to elastic and plastic anisotropy. For materials with similar elastic moduli, continuous increase of lattice strain signifies higher elastic stresses and the ability to sustain plastic flow at higher loadings. For the current VCoNi, all lattice strains have the same trend at both temperatures; all exhibit a continuously increasing trend with the macroscopic true strain. The only difference is the lattice strain magnitudes. The lattice strains ε_{200} and ε_{400} reach 1.2 % and 1.8 % at RT and 15 K, respectively. For all planes, the ultimate lattice strains (elastic) at 15 K are ~50 % higher than that at RT, corroborating the ~40 % increase in σ_u at 15 K. This behavior has been consistently observed in previous studies [11,13,26,28,30,31]. Throughout the entire deformation process and at both RT and 15 K, the magnitudes of lattice strains in different crystallographic planes are consistent with their respective elastic moduli E_{hkl} fit to ε_{hkl} within the elastic region (Table 2). For example, the ⟨111⟩ and ⟨100⟩ directions are the most and least stiff directions, respectively. The lattice strains ε_{111} and ε_{200} are the smallest and largest, respectively. In addition, lattice strains from their second-order reflections follow closely with the primary ones, e.g., ε_{222} and ε_{400} nearly overlap with ε_{111} and ε_{200}, respectively. The {111} and {222} planes remain less affected; ε_{111} and ε_{222} increase linearly throughout the plastic deformation process [32]. The stacking fault probability (SFP) can be estimated from the divergence in ε_{111} and ε_{222} by $SFP = \frac{32\pi}{3\sqrt{3}}(\varepsilon_{222} - \varepsilon_{111})$, see Ref. [33]. SFP can thus be tracked robustly from *in situ* diffractions, as demonstrated in numerous experiments [11,13,18,21,26,28,30,31,34–39]. Fig. 3c shows that the SFP at RT as well as 15 K remains negligibly small. The evolution of ε_{111} and ε_{222} of VCoNi is compared with that of other fcc M/HEAs in Fig. 4, where the diffraction data of CrCoNi, CrFeCoNi and CrMnFeCoNi were obtained from experiments conducted in a similar way at the TAKUMI beamline, J-PARC [11,13,26]. In contrast to other fcc M/HEAs such as the Cantor alloy where the differences in ε_{111} and ε_{222} and hence the SFP increase with deformation at cryogenic temperatures [11], VCoNi does not show discernible differences between the lattice strains of the {111} and {222} planes; ε_{111} and ε_{222} perfectly overlap throughout the entire deformation process at both RT and 15 K in Fig. 3. For VCoNi, the lattice strains for both {111} and {222} vary nearly linearly all the way to fracture (Fig. 4). For other alloys in Fig. 4, the linear relationship breaks down when the materials yielded and the deviation from the linear relationship becomes more pronounced at ultralow temperature. This goes to show that VCoNi is different from all other fcc M/HEAs. From these experimental data, we can unequivocally conclude that no extensive SFs are formed in VCoNi during deformation at both temperatures, consistent with previous post-mortem TEM studies [22,40].

Fig. 5 shows the evolution of the neutron diffraction peak intensities normalized by their respective values prior to deformation. Throughout the deformation, the peak intensities are quite similar at RT and 15 K. The intensities of the {111} planes increase almost linearly with the deformation after plastic yield, indicating that the grains along the {111} planes continuously rotate towards the LD. This grain rotation is typical in dislocation-dominated deformation in other fcc alloys, e.g., austenitic stainless steel and HEAs when the SFP is negligibly small [11,41]. However, for these alloys, when the SFP becomes significantly higher during low-temperature deformation, the {111} texture development slows down due to the activation of additional deformation mechanisms [11,13,28,31]. In contrast, VCoNi shows nearly the same texture development during deformation at RT and 15 K (Fig. 5a and b), with no signs of slowing down. The above results further suggest that the dominant deformation mechanism is dislocation glide at both temperatures.

Table 1
Mechanical properties of VCoNi at 293 K and 15 K. The yield strength (σ_y), ultimate tensile strength (σ_u), fracture strain (ε_f) and Young's modulus (E), all increase at 15 K.

Temperature (K)	σ_y (MPa)	σ_u (MPa)	ε_f (%)	E (GPa)
293 K	438	949	60.8	217
15 K	746	1325	73.2	233

3.3. Dislocation density and microstructure development

To assess the evolution of dislocation density ρ, diffraction peak

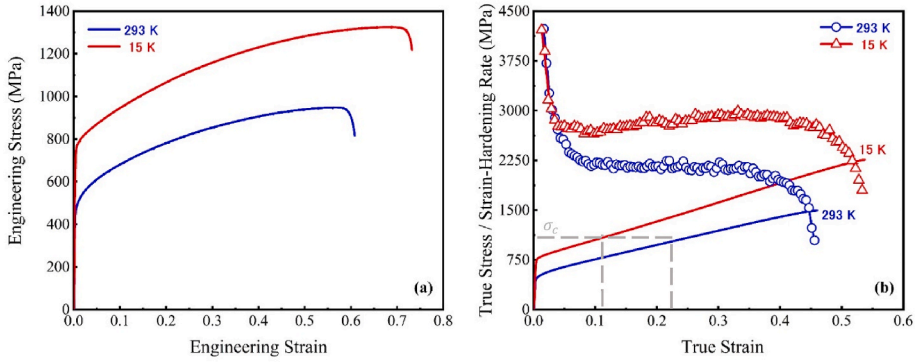

Fig. 2. Mechanical behavior of VCoNi at 293 K and 15 K. (a) The tensile engineering stress−strain curves. (b) The corresponding strain-hardening rates (hollow symbols) superimposed on the true stress-true strain curves (solid lines). The alloy shows enhanced mechanical properties at 15 K. σ_c is the characteristic stress related to ε_c in Fig. 6.

Table 2
Elastic properties of VCoNi at 293 K and 15 K. Elastic moduli along different lattice orientations (E_{hkl}), elastic anisotropy factor (E_{111}/E_{200}), lattice parameter (a_0), and overall elastic modulus of alloy (E_{fcc}), compared at two temperatures.

Temperature (K)	E_{111} (GPa)	E_{200} (GPa)	E_{220} (GPa)	E_{311} (GPa)	E_{111}/E_{200} (−)	a_0 (Å)	E_{fcc} (GPa)
293 K	233.0	147.9	203.0	176.8	1.575	3.6007	201
15 K	258.7	165.2	223.9	201.8	1.566	3.5933	211

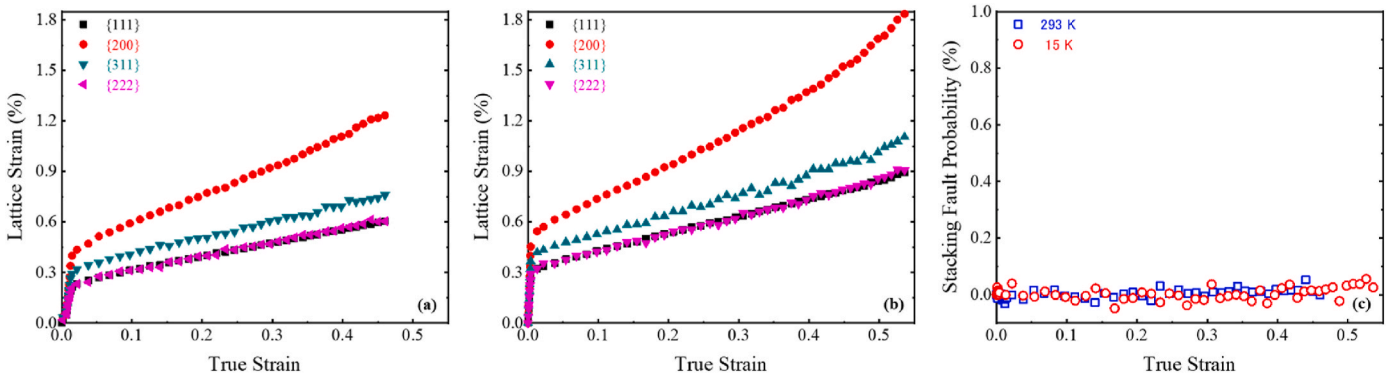

Fig. 3. Evolution of lattice strains and stacking fault probability for VCoNi. The lattice strain development along different {hkl} family of planes with deformation during uniaxial tensile loadings at (a) 293 K and (b) 15 K. (c) The stacking fault probability at both temperatures is negligibly small (remains close to zero).

broadening was analyzed using the Convolutional Multiple Whole Profile (CMWP) fitting, a modified Williamson−Hall method [42]. Fig. 6 shows ρ vs. ε during tensile deformation at RT and 15 K. In the early-stage straining $0 < \varepsilon < 0.05$, both samples have nearly identical initial dislocation densities ($\sim 3\times\ 10^{14}$ m^{-2}) and exhibit similar, gradual increases in ρ and strain-hardening rates $\frac{d\sigma}{d\varepsilon}$. Change in ρ diverges at $\varepsilon > 0.05$ at the two temperatures. In fact, the ρ evolution exhibits two distinct stages characterized by their respective nearly-constant but different accumulation rates $\frac{d\rho}{d\varepsilon}$. At 15 K, the transition between the two stages occurs at $0.05 < \varepsilon < 0.15$, with $\frac{d\rho}{d\varepsilon}$ nearly tripling from $9.5\times\ 10^{14}$ to 29.3×10^{14} m^{-2}. The high rate $\frac{d\rho}{d\varepsilon}$ is maintained until $\varepsilon = 0.42$ where ρ reaches 10^{16} m^{-2}. The rate-increase drops slightly afterwards, indicating dislocation density saturation and potential onset of dynamic recovery. The variation in $\frac{d\rho}{d\varepsilon}$ corresponds well to that in the strain-hardening rate $\frac{d\sigma}{d\varepsilon}$ (Fig. 2b); both $\frac{d\rho}{d\varepsilon}$ and $\frac{d\sigma}{d\varepsilon}$ exhibit a transition at $0.05 < \varepsilon < 0.15$, remain steady and near-constant at $0.15 < \varepsilon < 0.42$, and drops after $\varepsilon > 0.42$. Strain-hardening rate $\frac{d\sigma}{d\varepsilon}$ is thus closely associated with the dislocation density evolution rate $\frac{d\rho}{d\varepsilon}$. At RT, deformation starts with a low dislocation accumulation rate $\frac{d\rho}{d\varepsilon} = 9.8 \times 10^{14}$ m^{-2}, which is similar to the initial rate at 15 K. The low rate is maintained up to $\varepsilon = 0.10$, followed by a transition in $0.10 < \varepsilon < 0.30$, and reaches a near-constant value of 26.4×10^{14} m^{-2}, which is again similar to that in the high-rate regime at 15 K. The transition in $\frac{d\rho}{d\varepsilon}$ also manifests in the corresponding strain-hardening rate $\frac{d\sigma}{d\varepsilon}$ (Fig. 2b), albeit less distinct than that at 15 K.

The major difference between the two data sets in Fig. 6 lies in the strain range where the transition takes place. At 15 K, the transition occurs earlier at $\varepsilon \in [0.05, 0.15]$, indicating faster dislocation accumulation. At RT, the transition happens later at $\varepsilon \in [0.10, 0.30]$. The dislocation accumulation rates are fairly similar after their respective transitions complete. Within $0.25 < \varepsilon < 0.42$, the difference in ρ is nearly constant. Furthermore, the characteristic stresses σ_c at ε_c, where ε_c is defined by the intersection of the two $\frac{d\rho}{d\varepsilon}$ rates (Fig. 6), are nearly identical for the two temperatures (Fig. 2b), which in turn suggests that the transition is a stress-driven process. The sample at 15 K also has a higher tensile failure strain ε_f and exhibits almost twice the dislocation density of the sample deformed at RT. Overall, $\frac{d\rho}{d\varepsilon}$ has a weak

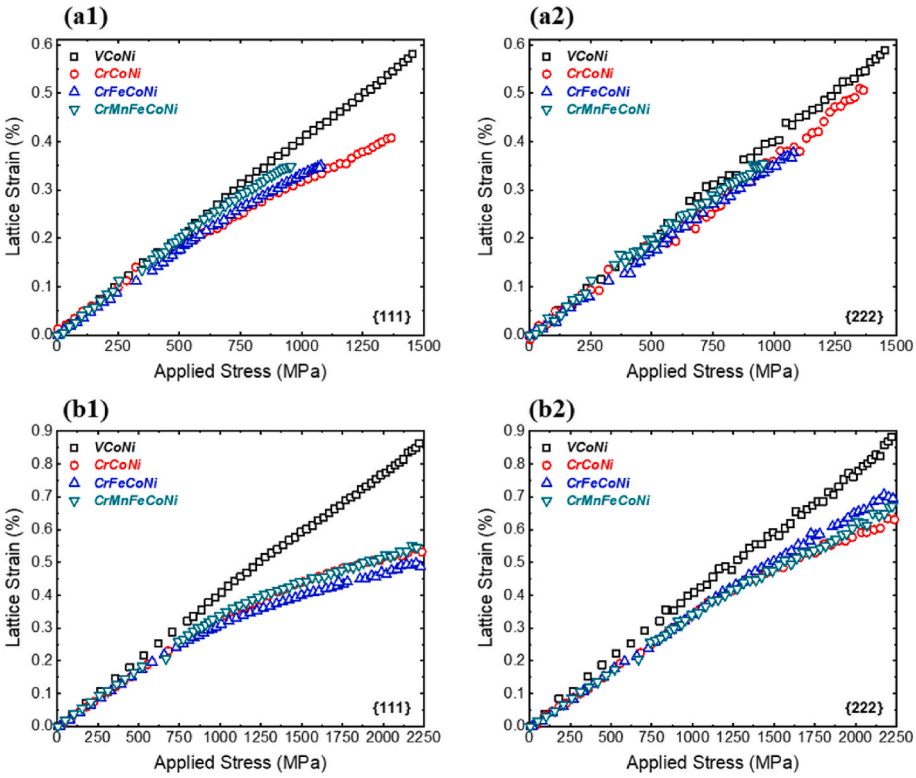

Fig. 4. Comparison of the lattice strains development for four fcc medium- and high-entropy alloys for {111} and {222} lattice planes at room temperature (a1 & a2) and ultralow temperature (b1 & b2). The lattice strain for VCoNi develops linearly at both temperatures. However, for other systems (i.e., CrCoNi, CrFeCoNi and CrMnFeCoNi), the lattice strain for {111} has lower values and non-linear trends at the same applied stress even at room temperature due to the development of stacking faults. The difference between the VCoNi and the other alloys becomes more prominent at ultralow temperature when stacking fault probability becomes significant for other alloys.

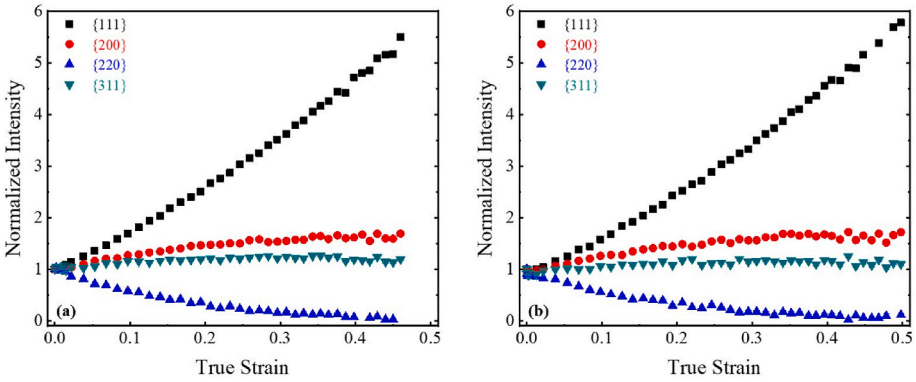

Fig. 5. Texture development in terms of integrated peak intensities during uniaxial tensile deformation for VCoNi at (a) 293 K and (b) 15 K. The peak intensities are normalized by the respective intensities before loading.

temperature-dependence in the two regimes. The evolutions of $\frac{d\rho}{d\varepsilon}$ and corresponding $\frac{d\sigma}{d\varepsilon}$ are largely similar at both temperatures; both exhibit characteristics typical in plastic deformation of fcc metals and alloys [13,43,44]. Taken together, these results suggest that faster generation and accumulation of dislocations drive the high strain hardening, stable plastic flow and ultimately enhanced strain-to-failure in the sample deformed at 15 K.

Transmission electron microscopy (TEM) was used to reveal lattice defects, including the expected high dislocation density, and to verify the dominant deformation mechanism at RT and 15 K. Nano-deformation bands within grains were found in the deformed VCoNi alloy at both temperatures. Fig. 7a shows the TEM image with the selected area electron diffraction (SAED) pattern at RT. Deformation bands are commonly formed as a result of the accumulation of high-density, statistically stored dislocations (SSDs), which posteriorly evolve into dense dislocation walls after medium-level strains [45]. With increasing strain, dislocation walls can rearrange into dislocation cells and form new boundaries. Fig. 7b shows a zone with a high density of SSDs bordering the contour of a nano-deformation band at 15 K. Similar nano-deformation bands have been reported in other plastically deformed alloys [45–47]. No other lattice faults, such as deformation twin boundaries, SFs, or hcp-martensite, are observed during deformation. Fig. 7c and d shows the corresponding deformation micro-mechanisms at RT and 15 K, respectively. At room temperature, the deformation is dominated by the planar slip of ½ [110] dislocations (Fig. 7c). In contrast, at 15 K, the deformation results in a dislocation cell

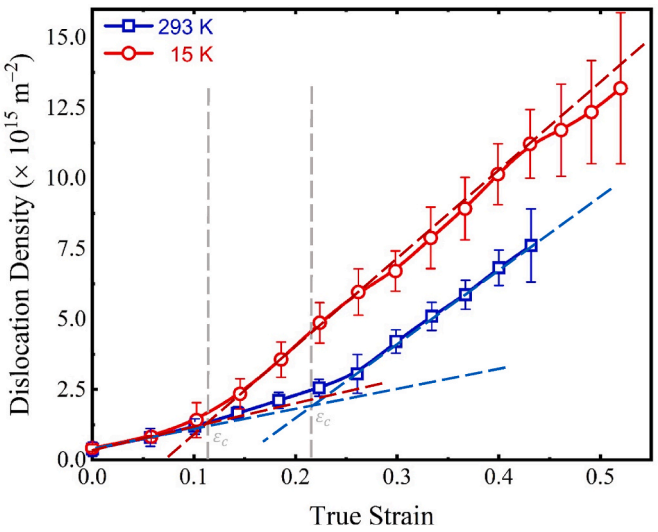

Fig. 6. Evolution of dislocation densities during tensile deformation at 293 K and 15 K. Both samples exhibit a two-stage dislocation density accumulation with similar slopes $\frac{d\rho}{d\varepsilon}$, but at 12 % and 22 % strains (ε_c) in the 15 K and RT samples, respectively.

structure with highly tangled dislocations (Fig. 7d).

The electron backscatter diffraction (EBSD) maps in Fig. 8 show grain boundary misorientation, inverse pole figure (IPF), and geometrically necessary dislocation (GND) maps before and after deformation at RT and 15 K. The EBSD scanning is done along a plane parallel to the LD. Annealing twins are present prior to deformation, as evident from their characteristic nearly-straight boundaries across the grains or blunt ends. The undeformed sample has a weak texture with a nearly random grain orientation (Fig. 8a1). After deformation, annealing twins remain and a large number of grains rotated towards the [111] and [001] directions (Fig. 8a2 & a3), in agreement with the increase in the integrated peak intensities of the {111} and {200} planes (Fig. 5). These changes of grain orientations are typical in fcc materials when plastic strain is carried out by dislocation glides [48], and it agrees with the increasing GND density before (Fig. 8b1) and after (Fig. 8b2 & b3) deformation at RT and 15 K, respectively. These results, together with the formation of nano-bands, the negligible SFP (Fig. 3c) and dislocation density evolution (Fig. 6), suggest that no new twins are formed during deformation. Therefore, dislocation glide is the primary plastic deformation mechanism in the present VCoNi multi-principal element alloy deformed at both temperatures.

4. Discussion

The combined *in situ* neutron diffraction and *ex situ* TEM study uncovers the deformation characteristics, dislocation and microstructure evolution in VCoNi alloy. Here, the plastic deformation is dominated by dislocation glide at both temperatures. Moreover, dislocations accumulate faster at 15 K. These results can be reconciled by considering the Orowan equation governing the dislocation dynamics [49].

In VCoNi, V has a large misfit volume and preferentially forms V-Cr and V-Ni neighboring pairs [20], which in return induce significant lattice distortion [22] and a high lattice friction/energy barrier ΔE_B to dislocation glide. In solid solution alloys, ΔE_B varies with local solute environment. For the general discussion, we consider the mean energy

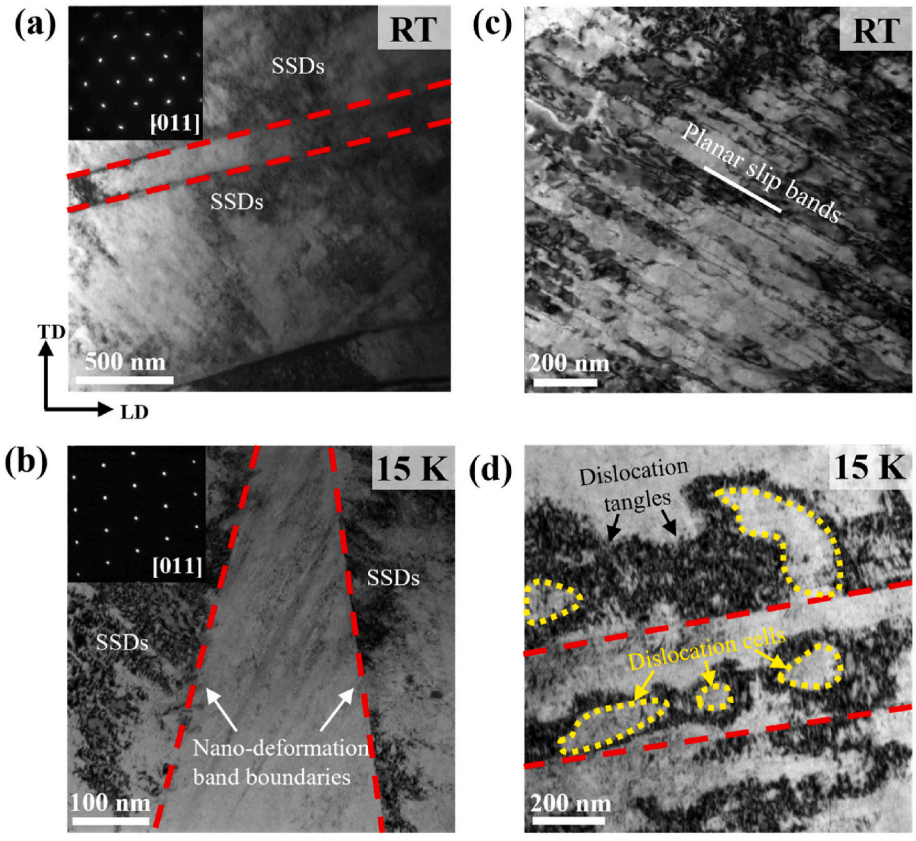

Fig. 7. Deformation micro-mechanisms at RT and 15 K. (a, b) TEM micrographs revealing nano-deformation band (highlighted in red) with SSDs along the border and the corresponding SAED patterns at RT and 15 K, respectively. (c) Planar dislocation structures observed at RT after deformation. (d) Dislocation cell network formation at 15 K after deformation, showing high-density dislocation tangles (black arrows), cells (yellow dashed regions) and nano-deformation bands (red dashed lines) formed by thick SSD walls. (For interpretation of the references to colour in this figure legend, the reader is referred to the Web version of this article.)

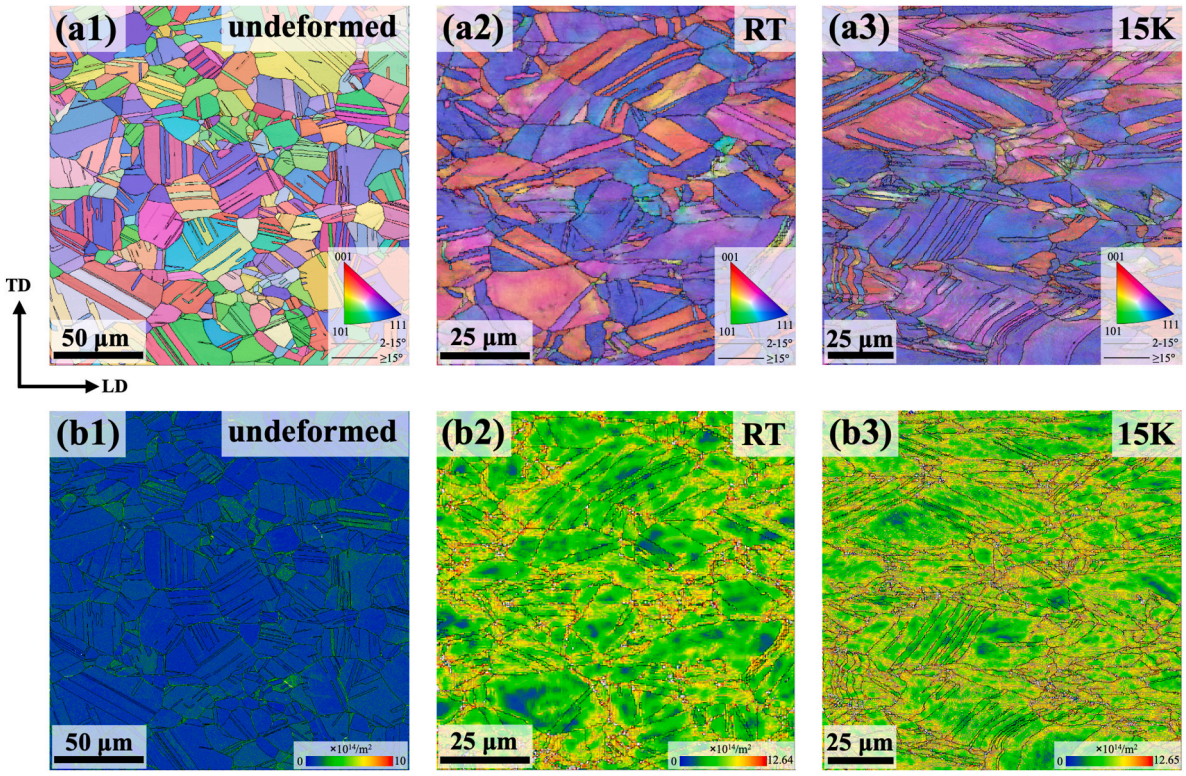

Fig. 8. Microstructure evolution before deformation and after fracture at different temperatures. EBSD IPF maps with image quality maps overlapped (upper panels), and the corresponding GND maps (lower panels) showing low and high angle grain boundaries, annealing twins and orientation of the crystal with respect to the loading direction: (a1, b1) before deformation, and after fracture, at (a2, b2) room temperature and (a3, b3) 15 K, respectively.

barrier as [50]

$$\Delta E_B = b \int (\tau_{PS} - \tau_{app}) dA \tag{1}$$

where b is the magnitude of Burgers vector, τ_{PS} and τ_{app} are the Peierls stress and applied stress, and A is the activation area. The mean rate $\bar{\nu}_L$ of dislocation overcoming the local barriers can be expressed by the Arrhenius equation [51]

$$\bar{\nu}_L = \nu_0 \exp\left(\frac{-\Delta E_B}{kT}\right) = \nu_0 \exp\left(\frac{-b \int (\tau_{PS} - \tau_{app}) dA}{kT}\right) \tag{2}$$

where ν_0 is the attempt frequency and k is the Boltzmann constant. It can be seen, therefore, that the thermal activation term kT and applied load τ_{app} have similar effects in maintaining $\bar{\nu}_L$. Larger thermal activation reduces the required τ_{app} and the apparent critical resolved shear stress (CRSS) at the same $\bar{\nu}_L$ or strain rate $\dot{\varepsilon}$ [52,53], as prescribed by the Orowan equation [54,55]

$$\dot{\varepsilon} = \rho_m b \bar{\nu}_L L \tag{3}$$

where ρ_m and L are the mobile dislocation density and mean distance between the barriers.

During the initial yielding and in the low-strain regime, the yield and early flow stresses (σ_y and σ_f) are governed by individual dislocations overcoming their local barriers created by the underlying distorted lattice/chemical species interactions. In the current VCoNi, the initial ρ_m and L are similar in the two samples deformed at RT and 15 K, since they were produced by the same thermo-mechanical processing route. The sample at 15 K naturally exhibits a higher yield strength than that at RT, because a larger τ_{app} is needed to drive dislocations to satisfy the same imposed $\dot{\varepsilon}/\bar{\nu}_L$. The effects of temperature thus manifest in $\Delta\sigma_y$ at these two temperatures (Fig. 2a), as is well-known for a broad range of metals and alloys.

More importantly, the Orowan equation also shows that increasing ρ_m can meet the constant $\dot{\varepsilon}$ at lower τ_{app} or kT. Deformation at very low T thus tends to activate more dislocation sources or slip systems, and eventually exhibits faster dislocation accumulation rate $\frac{d\rho}{d\varepsilon}$. The initial lattice friction ΔE_B-limited yielding stage can only last within a small strain range $\varepsilon < 0.05$, corresponding to the strains where the dislocation densities are indistinguishable in the RT and 15 K samples (Fig. 6) and both hardening rates drop rapidly (Fig. 2b). With increasing ε and ρ, dislocation interactions become stronger as a result of their elastic interactions and the formation of jogs and sessile locks [56]. Continuous dislocation glide thus needs to overcome the lattice friction ΔE_B, as well as the dynamically-created junction barriers. At 15 K, jogs and locks are more difficult to overcome [57]. With increasing τ_{app}, multi-slips have to be activated, which in turn creates more jogs, locks, and increases dislocation density. The increase in overall dislocation density further creates more dislocation jogs and locks. A self-catalyzing process is thus established quickly, leading to the earlier and quicker switch of the rate-limiting mechanism ($0.05 < \varepsilon < 0.15$) from lattice-friction dominated to dislocation-interaction/forest-hardening dominated. With this switch, the Orowan equation has a modified form [54,55]

$$\dot{\varepsilon} = \rho_m b \bar{\nu}_{esc} L_f \tag{4}$$

where L_f is the mean distance between jogs/locks and is proportional to $1/\sqrt{\rho}$ in general, and $\bar{\nu}_{esc}$ is the escape rate for dislocations breaking away from obstacles created by forest dislocations. The escape rate again depends on the applied stress and the temperature [58], as well as the dislocation interaction strength, i.e.,

$$\bar{\nu}_{esc} \propto \exp\left\{\frac{-G_0}{kT}\left[1 - \left(\frac{\tau_{app}}{\tau_c}\right)^p\right]^q\right\} \tag{5}$$

where G_0, p, q are material-dependent parameters for the escape energy profile and τ_c is the critical stress to activate the slip system. These

material-specific properties do not change the overall plastic behavior in Stage II deformation, which typically exhibits a nearly-constant hardening rate $\frac{d\sigma}{d\varepsilon} \propto \alpha\mu$ (Fig. 2b), where α and μ are a scaling factor and the shear modulus, respectively. At RT, deformation is carried out by single slip for an extended range of strains as the secondary barriers have weaker effects and the self-catalyzing process is established more slowly. The switch from single-slip to multi-slip and the corresponding rate-limiting mechanisms thus initiate at larger strains and completes over a wider range. Despite these differences, the evolutions of strain hardening $\frac{d\sigma}{d\varepsilon}$ and dislocation accumulation $\frac{d\rho}{d\varepsilon}$ exhibit similar patterns and weak temperature-dependence. Furthermore, the switch from single-slip to multi-slip is also evident in TEM observations in M/HEAs and the current VCoNi where multi-slip is more pronounced at higher strains [9,40,59]. The increased dislocation-driven strain hardening rate prevents plastic instability and enables continued uniform tensile deformation. This effect is more pronounced with decreasing temperature, because $\bar{\nu}_{esc}$ decreases as kT approaches zero, leading to a *simultaneous increase* in strength and ductility and enhanced mechanical properties at ultralow temperatures. That being the case, the low-temperature deformation mechanism in VCoNi is thus distinctly different from those known in other fcc M/HEAs [6,10–14], where SF/twin/martensitic transformation becomes increasingly important as the temperature is lowered.

The above discussion is general and does not involve any material-specific properties. It is applicable to fcc metals and alloys where deformation is carried out by dislocation plasticity. This suggests a simultaneous increase of strength and ductility with decreasing temperature should be quite general in the fcc family, even in the absence of TWIP/TRIP effects. However, as previously highlighted, there can be significant variations in strain-hardening behaviors for the same fcc alloy. For instance, at 15 K, there is a relatively constant strain-hardening rate of ~2.9 GPa (Fig. 2b). The corresponding findings presented in this study can hence be interpreted by comparing the deformation micro-mechanisms of the VCoNi at varying temperatures with those characteristic of single-fcc phase M/HEAs exhibiting high SFE.

At room temperature, the dislocation motion in VCoNi is highly planar in nature, as observed in Fig. 7c. Similar deformation micro-mechanisms are observed at 15 K, although the nano-deformation bands exhibit reduced width compared to those at RT (Fig. 7b). This decrease in boundary spacing can be attributed to the enhanced strain localization near fracture at 15 K, consistent with observations in pure nickel [45]. Interestingly, as the temperature decreases, the cellular dislocation microstructure becomes prominent, with varying dislocation densities observed in the cell interiors and cell walls (Fig. 7d). These differences in micro-mechanisms at different temperatures are crucial in comprehending the strain-hardening and deformation behavior of VCoNi. As mentioned previously, the earlier transition (~0.12 of true strain) from single-to multi-slip at 15 K intensifies the heterogeneity of dislocation distribution, resulting in the development of dislocation cells with the majority of dislocations located in cell walls [60]. Though multi-slip is not necessary for cell formation in high SFE materials, the absence of dislocation cells at RT, despite the later transition (~0.22 of true strain) in slip modes, suggests limited cross-slip in VCoNi even at elevated temperatures [61,62]. Indeed, a wide range of experiments on low and high SFE fcc metals and alloys, conducted in the past and recent years, demonstrated enhanced strength−ductility combination at lower temperatures. Such examples include 99.999%-pure Cu [23], 99.99%-pure Al [24], 99.85%-pure Al, solid solution Al-Mg and precipitation-strengthened Al alloy [63], commercial AA1050, commercially pure Cu and Cu-15Zn alloy [44], AA6060 Al alloys [25], 99.9995%-pure Al and AA5754 Al alloys [64], 99.95%-pure Cu [65]. Among them, high-purity, low SFE Cu and high SFE Al develop dislocation cell-networks without twinning after deformation at 77 K [65] and 4.2 K [64]. Such cell-networks are similar to that in VCoNi deformed at 15 K (Fig. 7), as well as those at 77 K and 4.2 K [22]. It goes to further suggest that the dislocation-based enhanced hardening mechanism is not sensitive to SFE. The key for dislocation-mediated plasticity to operate includes the following: (i) the ability to generate and store a high density of dislocations during early-stages of deformation and (ii) the prevention of other unstable plastic deformation modes such as brittle cleavage at grain/phase boundaries. It is worthwhile to note that these requirements are generally satisfied in fcc metals and alloys. In the present VCoNi, the high lattice friction can further delay dynamic recovery and enhance dislocation accumulation/storage (Fig. 6).

Finally, the apparent lack of stacking fault, deformation twinning, or martensitic phase transformation is intriguing. SRO may have played an important role in governing deformation and phase stability in VCoNi. Recent DFT results show that SRO increases the mean SFE of VCoNi to 226 mJ/m^2, which reduces its deformation twinnability to levels lower than any elemental fcc metals [20]. In addition, SRO also increases the energy difference $\Delta E_{hcp-fcc}$ from near 0 to above 30 meV/atom, which in turn makes the hcp phase less favorable. Therefore, neither deformation twinning nor fcc-to-hcp martensitic phase transformation is expected in VCoNi during both RT and 15 K deformation. This prediction is consistent with the measured SFP (Figs. 3 and 4), TEM images (Fig. 7), the evolutions of peak intensities (Fig. 5), dislocation density evolution (Fig. 6) and EBSD texture (Fig. 8), as well as all deformation experiments in VCoNi performed up to date [22,40,62].

5. Conclusions

In summary, we studied the mechanical behavior of VCoNi multi-principal element alloy at RT and 15 K. *In situ* neutron diffraction provided critical information on the lattice strain, texture, and dislocation density evolution throughout the entire deformation process. The current results provide unequivocal evidence that the plastic deformation at both temperatures is carried out primarily by dislocation glide and shares many common features. Strain hardening is closely related to dislocation density and a two-stage dislocation accumulation is revealed at both temperatures. The enhanced mechanical properties at cryogenic temperatures can thus be explained based on classical dislocation mechanism alone, in the absence of TWIP/TRIP effects. Therefore, the physical mechanism corresponding to the two-stage, slow/single-slip and fast/multi-slip dislocation accumulation comprises a key component to understand and control mechanical behaviors of complex alloys.

CRediT authorship contribution statement

Muhammad Naeem: Writing – review & editing, Writing – original draft, Methodology, Investigation, Formal analysis, Conceptualization. **Yuemin Ma:** Writing – review & editing, Visualization, Methodology, Investigation, Formal analysis. **Jin Tian:** Writing – review & editing, Visualization, Methodology, Investigation, Formal analysis. **Haojie Kong:** Writing – review & editing, Methodology, Investigation. **Liliana Romero-Resendiz:** Writing – review & editing, Visualization, Validation, Methodology, Investigation, Formal analysis. **Ziyang Fan:** Writing – review & editing, Methodology, Data curation. **Feng Jiang:** Resources, Methodology. **Wu Gong:** Writing – review & editing, Methodology. **Stefanus Harjo:** Writing – review & editing, Methodology. **Zhaoxuan Wu:** Writing – original draft, Validation. **Xun-Li Wang:** Writing – review & editing, Validation, Supervision, Resources, Funding acquisition.

Data availability

Data will be made available on request.

Declaration of competing interest

The authors declare that they have no known competing financial interests or personal relationships that could have appeared to influence the work reported in this paper.

Acknowledgments

We acknowledge the funding support from the Research Grants Council of Hong Kong Special Administrative Region (C1020-21G). X.L. W thank the Croucher Foundation for the Croucher Senior Research Fellowship (CityU 9509008) and Shenzhen Science and Technology Program (Project No. JCYJ20220818101203007). M.N. thanks the Asia-Oceania Neutron Scattering Association (AONSA) for the award of AONSA Young Research Fellowship (AONSA-YRF-2022). The neutron diffraction experiments were conducted at TAKUMI Engineering Materials Diffractometer (BL19) of the Materials and Life Science Experimental Facility at J-PARC Center under the user program (proposal number 2020A0185).

References

[1] J.-W. Yeh, S.-K. Chen, S.-J. Lin, J.-Y. Gan, T.-S. Chin, T.-T. Shun, C.-H. Tsau, S.-Y. Chang, Nanostructured high-entropy alloys with multiple Principal elements: novel alloy Design Concepts and Outcomes, Adv. Eng. Mater. 6 (2004) 299–303, https://doi.org/10.1002/adem.200300567.

[2] W.-L. Hsu, C.-W. Tsai, A.-C. Yeh, J.-W. Yeh, Clarifying the four core effects of high-entropy materials, Nat. Rev. Chem 8 (2024) 471–485, https://doi.org/10.1038/s41570-024-00602-5.

[3] A. Fu, B. Liu, W. Lu, B. Liu, J. Li, Q. Fang, Z. Li, Y. Liu, A novel supersaturated medium entropy alloy with superior tensile properties and corrosion resistance, Scr Mater 186 (2020) 381–386, https://doi.org/10.1016/j.scriptamat.2020.05.023.

[4] J. Han, Y. Zhang, Z. Sun, Y. Zhang, Y. Zhao, L. Sun, Z. Zhang, Enhanced irradiation tolerance of a medium entropy alloy via precipitation and dissolution of nanoprecipitates, J. Nucl. Mater. 586 (2023) 154693, https://doi.org/10.1016/j.jnucmat.2023.154693.

[5] F. Cao, P. Munroe, Z. Zhou, Z. Xie, Medium entropy alloy CoCrNi coatings: Enhancing hardness and damage-tolerance through a nanotwinned structuring, Surf. Coat. Technol. 335 (2018) 257–264, https://doi.org/10.1016/j.surfcoat.2017.12.021.

[6] B. Gludovatz, A. Hohenwarter, K.V.S. Thurston, H. Bei, Z. Wu, E.P. George, R. O. Ritchie, Exceptional damage-tolerance of a medium-entropy alloy CrCoNi at cryogenic temperatures, Nat. Commun. 7 (2016) 10602, https://doi.org/10.1038/ncomms10602.

[7] Z. Zhang, H. Sheng, Z. Wang, B. Gludovatz, Z. Zhang, E.P. George, Q. Yu, S.X. Mao, R.O. Ritchie, Dislocation mechanisms and 3D twin architectures generate exceptional strength-ductility-toughness combination in CrCoNi medium-entropy alloy, Nat. Commun. 8 (2017) 14390, https://doi.org/10.1038/ncomms14390.

[8] G. Laplanche, A. Kostka, C. Reinhart, J. Hunfeld, G. Eggeler, E.P. George, Reasons for the superior mechanical properties of medium-entropy CrCoNi compared to high-entropy CrMnFeCoNi, Acta Mater. 128 (2017) 292–303, https://doi.org/10.1016/j.actamat.2017.02.036.

[9] S.S. Sohn, A. Kwiatkowski da Silva, Y. Ikeda, F. Körmann, W. Lu, W.S. Choi, B. Gault, D. Ponge, J. Neugebauer, D. Raabe, Ultrastrong medium-entropy single-phase alloys Designed via severe lattice distortion, Adv Mater 31 (2019) 1807142, https://doi.org/10.1002/adma.201807142.

[10] B. Gludovatz, A. Hohenwarter, D. Catoor, E.H. Chang, E.P. George, R.O. Ritchie, A fracture-resistant high-entropy alloy for cryogenic applications, Science 345 (2014) 1153–1158, https://doi.org/10.1126/science.1254581.

[11] M. Naeem, H. He, F. Zhang, H. Huang, S. Harjo, T. Kawasaki, B. Wang, S. Lan, Z. Wu, F. Wang, Y. Wu, Z. Lu, Z. Zhang, C.T. Liu, X.-L. Wang, Cooperative deformation in high-entropy alloys at ultralow temperatures, Sci. Adv. 6 (2020), https://doi.org/10.1126/sciadv.aax4002 eaax4002.

[12] J. Moon, E. Tabachnikova, S. Shumilin, T. Hryhorova, Y. Estrin, J. Brechtl, P. K. Liaw, W. Wang, K.A. Dahmen, A. Zargaran, J.W. Bae, H.-S. Do, B.-J. Lee, H. S. Kim, Deformation behavior of a Co-Cr-Fe-Ni-Mo medium-entropy alloy at extremely low temperatures, Mater. Today 50 (2021) 55–68, https://doi.org/10.1016/j.mattod.2021.08.001.

[13] M. Naeem, H. He, S. Harjo, T. Kawasaki, W. Lin, J.-J. Kai, Z. Wu, S. Lan, X.-L. Wang, Temperature-dependent hardening contributions in CrFeCoNi high-entropy alloy, Acta Mater. 221 (2021) 117371, https://doi.org/10.1016/j.actamat.2021.117371.

[14] Y.H. Jo, S. Jung, W.M. Choi, S.S. Sohn, H.S. Kim, B.J. Lee, N.J. Kim, S. Lee, Cryogenic strength improvement by utilizing room-temperature deformation twinning in a partially recrystallized VCrMnFeCoNi high-entropy alloy, Nat. Commun. 8 (2017) 15719, https://doi.org/10.1038/ncomms15719.

[15] K.V.S. Thurston, A. Hohenwarter, G. Laplanche, E.P. George, B. Gludovatz, R. O. Ritchie, On the onset of deformation twinning in the CrFeMnCoNi high-entropy alloy using a novel tensile specimen geometry, Intermetallics 110 (2019) 106469, https://doi.org/10.1016/j.intermet.2019.04.012.

[16] M. Schneider, G. Laplanche, Effects of temperature on mechanical properties and deformation mechanisms of the equiatomic CrFeNi medium-entropy alloy, Acta Mater. 204 (2021) 116470, https://doi.org/10.1016/j.actamat.2020.11.012.

[17] F. Otto, A. Dlouhý, Ch Somsen, H. Bei, G. Eggeler, E.P. George, The influences of temperature and microstructure on the tensile properties of a CoCrFeMnNi high-entropy alloy, Acta Mater. 61 (2013) 5743–5755, https://doi.org/10.1016/j.actamat.2013.06.018.

[18] Y. Ma, M. Naeem, L. Zhu, H. He, X. Sun, Z. Yang, F. He, S. Harjo, T. Kawasaki, X.-L. Wang, Microscopic insights of the extraordinary work-hardening due to phase transformation, Acta Mater. 270 (2024) 119822, https://doi.org/10.1016/j.actamat.2024.119822.

[19] S. Huang, W. Li, S. Lu, F. Tian, J. Shen, E. Holmström, L. Vitos, Temperature dependent stacking fault energy of FeCrCoNiMn high entropy alloy, Scr Mater 108 (2015) 44–47, https://doi.org/10.1016/j.scriptamat.2015.05.041.

[20] L. Zhu, Z. Wu, Effects of short range ordering on the generalized stacking fault energy and deformation mechanisms in FCC multiprincipal element alloys, Acta Mater. 259 (2023) 119230, https://doi.org/10.1016/j.actamat.2023.119230.

[21] K.V. Werner, M. Naeem, F. Niessen, L. Zhu, M. Villa, X.-L. Wang, M.A.J. Somers, Experimental and computational assessment of the temperature dependency of the stacking fault energy in face-centered cubic high-entropy alloys, Acta Mater. 278 (2024) 120271, https://doi.org/10.1016/j.actamat.2024.120271.

[22] R.K. Nutor, T. Xu, X. Wang, X.-D. Wang, P. An, J. Zhang, T. Hu, L. Li, Q. Cao, S. Ding, D. Zhang, J.-Z. Jiang, Liquid helium temperature deformation and local atomic structure of CoNiV medium entropy alloy, Mater. Today Commun. 30 (2022) 103141, https://doi.org/10.1016/j.mtcomm.2022.103141.

[23] R.P. Carreker, W.R. Hibbard, Tensile deformation of high-purity copper as a function of temperature, strain rate, and grain size, Acta Metall. 1 (1953) 654–663, https://doi.org/10.1016/0001-6160(53)90022-4.

[24] W.F. Hosford, R.L. Fleischer, W.A. Backofen, Tensile deformation of aluminum single crystals at low temperatures, Acta Metall. 8 (1960) 187–199, https://doi.org/10.1016/0001-6160(60)90127-9.

[25] Z. Xu, H.J. Roven, Z. Jia, Mechanical properties and surface characteristics of an AA6060 alloy strained in tension at cryogenic and room temperature, Mater Sci Eng A 648 (2015) 350–358, https://doi.org/10.1016/j.msea.2015.09.083.

[26] H. He, M. Naeem, F. Zhang, Y. Zhao, S. Harjo, T. Kawasaki, B. Wang, X. Wu, S. Lan, Z. Wu, W. Yin, Y. Wu, Z. Lu, J.-J. Kai, C.-T. Liu, X.-L. Wang, Stacking Fault driven phase transformation in CrCoNi medium entropy alloy, Nano Lett. 21 (2021) 1419–1426, https://doi.org/10.1021/acs.nanolett.0c04244.

[27] T. Liu, Y. Gao, H. Bei, K. An, In situ neutron diffraction study on tensile deformation behavior of carbon-strengthened CoCrFeMnNi high-entropy alloys at room and elevated temperatures, J. Mater. Res. 33 (2018) 3192–3203, https://doi.org/10.1557/jmr.2018.180.

[28] Y. Wang, B. Liu, K. Yan, M. Wang, S. Kabra, Y.-L. Chiu, D. Dye, P.D. Lee, Y. Liu, B. Cai, Probing deformation mechanisms of a FeCoCrNi high-entropy alloy at 293 and 77 K using in situ neutron diffraction, Acta Mater. 154 (2018) 79–89, https://doi.org/10.1016/j.actamat.2018.05.013.

[29] H. Wang, Q. He, X. Gao, Y. Shang, W. Zhu, W. Zhao, Z. Chen, H. Gong, Y. Yang, Multifunctional high entropy alloys enabled by severe lattice distortion, Adv Mater 36 (2024) 2305453, https://doi.org/10.1002/adma.202305453.

[30] M. Naeem, H. Zhou, H. He, S. Harjo, T. Kawasaki, S. Lan, Z. Wu, Y. Zhu, X.-L. Wang, Martensitic transformation in CrCoNi medium-entropy alloy at cryogenic temperature, Appl. Phys. Lett. 119 (2021) 131901, https://doi.org/10.1063/5.0067268.

[31] L. Tang, L. Wang, M. Wang, H. Liu, S. Kabra, Y. Chiu, B. Cai, Synergistic deformation pathways in a TWIP steel at cryogenic temperatures: in situ neutron diffraction, Acta Mater. 200 (2020) 943–958, https://doi.org/10.1016/j.actamat.2020.09.075.

[32] B. Clausen, T. Lorentzen, T. Leffers, Self-consistent modelling of the plastic deformation of f.c.c. polycrystals and its implications for diffraction measurements of internal stresses, Acta Mater. 46 (1998) 3087–3098, https://doi.org/10.1016/S1359-6454(98)00014-7.

[33] B.E. Warren, X-Ray Diffraction, Dover Publications, 1990.

[34] J.S. Jeong, W. Woo, K.H. Oh, S.K. Kwon, Y.M. Koo, In situ neutron diffraction study of the microstructure and tensile deformation behavior in Al-added high manganese austenitic steels, Acta Mater. 60 (2012) 2290–2299, https://doi.org/10.1016/j.actamat.2011.12.043.

[35] B. Cai, B. Liu, S. Kabra, Y. Wang, K. Yan, P.D. Lee, Y. Liu, Deformation mechanisms of Mo alloyed FeCoCrNi high entropy alloy: in situ neutron diffraction, Acta Mater. 127 (2017) 471–480, https://doi.org/10.1016/j.actamat.2017.01.034.

[36] M. Naeem, H. He, S. Harjo, T. Kawasaki, F. Zhang, B. Wang, S. Lan, Z. Wu, Y. Wu, Z. Lu, C.T. Liu, X.-L. Wang, Extremely high dislocation density and deformation pathway of CrMnFeCoNi high entropy alloy at ultralow temperature, Scr Mater 188 (2020) 21–25, https://doi.org/10.1016/j.scriptamat.2020.07.004.

[37] Y.Y. Shang, Y. Wu, J.Y. He, X.Y. Zhu, S.F. Liu, H.L. Huang, K. An, Y. Chen, S. H. Jiang, H. Wang, X.J. Liu, Z.P. Lu, Solving the strength-ductility tradeoff in the medium-entropy NiCoCr alloy via interstitial strengthening of carbon, Intermetallics 106 (2019) 77–87, https://doi.org/10.1016/J.INTERMET.2018.12.009.

[38] W. Woo, J.S. Jeong, D.K. Kim, C.M. Lee, S.H. Choi, J.Y. Suh, S.Y. Lee, S. Harjo, T. Kawasaki, Stacking Fault energy Analyses of Additively Manufactured stainless steel 316L and CrCoNi medium entropy alloy using in situ neutron diffraction, Sci. Rep. 10 (2020) 1–15, https://doi.org/10.1038/s41598-020-58273-3.

[39] M. Frank, S.S. Nene, Y. Chen, S. Thapliyal, S. Shukla, K. Liu, S. Sinha, T. Wang, M. J. Frost, K. An, R.S. Mishra, Direct evidence of the stacking fault-mediated strain hardening phenomenon, Appl. Phys. Lett. 119 (2021) 081906, https://doi.org/10.1063/5.0062153.

[40] D.C. Yang, Y.H. Jo, Y. Ikeda, F. Körmann, S.S. Sohn, Effects of cryogenic temperature on tensile and impact properties in a medium-entropy VCoNi alloy, J. Mater. Sci. Technol. 90 (2021) 159–167, https://doi.org/10.1016/J.JMST.2021.02.034.

[41] E.-W. Huang, R. Barabash, N. Jia, Y.-D. Wang, G.E. Ice, B. Clausen, J. Horton, P. K. Liaw, Slip-system-related dislocation study from in-situ neutron measurements,

Metall. Mater. Trans. A 39 (2008) 3079–3088, https://doi.org/10.1007/s11661-008-9704-1.
[42] G. Ribárik, B. Jóni, T. Ungár, The Convolutional multiple Whole profile (CMWP) fitting method, a Global Optimization Procedure for microstructure Determination, Crystals 10 (2020) 623, https://doi.org/10.3390/cryst10070623.
[43] V.S. Sarma, J. Wang, W.W. Jian, A. Kauffmann, H. Conrad, J. Freudenberger, Y. T. Zhu, Role of stacking fault energy in strengthening due to cryo-deformation of FCC metals, Mater Sci Eng A 527 (2010) 7624–7630, https://doi.org/10.1016/j.msea.2010.08.015.
[44] D.C.C. Magalhães, A.M. Kliauga, M. Ferrante, V.L. Sordi, Plastic deformation of FCC alloys at cryogenic temperature: the effect of stacking-fault energy on microstructure and tensile behaviour, J. Mater. Sci. 52 (2017) 7466–7478, https://doi.org/10.1007/s10853-017-0979-8.
[45] D.A. Hughes, N. Hansen, Microstructure and strength of nickel at large strains, Acta Mater. 48 (2000) 2985–3004, https://doi.org/10.1016/S1359-6454(00)00082-3.
[46] H.W. Zhang, X. Huang, N. Hansen, Evolution of microstructural parameters and flow stresses toward limits in nickel deformed to ultra-high strains, Acta Mater. 56 (2008) 5451–5465, https://doi.org/10.1016/j.actamat.2008.07.040.
[47] B.L. Li, A. Godfrey, Q.C. Meng, Q. Liu, N. Hansen, Microstructural evolution of IF-steel during cold rolling, Acta Mater. 52 (2004) 1069–1081, https://doi.org/10.1016/j.actamat.2003.10.040.
[48] N. Hansen, D.J. Jensen, Development of microstructure in FCC metals during cold work, Philos Trans R Soc A 357 (1999) 1447–1469, https://doi.org/10.1098/rsta.1999.0384.
[49] E. Orowan, Discussion on internal stresses, in: Symposium on Internal Stresses in Metals and Alloys, The Institute of Metals, London, 1948, pp. 451–453.
[50] G.B. Gibbs, Thermodynamic analysis of dislocation glide controlled by dispersed local obstacles, Mater Sci Eng 4 (1969) 313–328, https://doi.org/10.1016/0025-5416(69)90026-3.
[51] A.S. Argon, Strengthening Mechanisms in Crystal Plasticity, Oxford University Press, 2008.
[52] Y.Y. Zhao, T.G. Nieh, Correlation between lattice distortion and friction stress in Ni-based equiatomic alloys, Intermetallics 86 (2017) 45–50, https://doi.org/10.1016/j.intermet.2017.03.011.
[53] C. Varvenne, A. Luque, W.A. Curtin, Theory of strengthening in fcc high entropy alloys, Acta Mater. 118 (2016) 164–176, https://doi.org/10.1016/j.actamat.2016.07.040.
[54] E.I. Galindo-Nava, C.M.F. Rae, Microstructure-sensitive modelling of dislocation creep in polycrystalline FCC alloys: Orowan theory revisited, Mater Sci Eng A 651 (2016) 116–126, https://doi.org/10.1016/j.msea.2015.10.088.
[55] E. Orowan, Problems of plastic gliding, Proc. Phys. Soc. 52 (1940) 8–22, https://doi.org/10.1088/0959-5309/52/1/303.
[56] F. Nabarro, J.P. Hirth, Dislocations in Solids, first ed., Elsevier, North-Holland, 2007. Netherlands.
[57] A.S. Tirunilai, T. Hanemann, K.P. Weiss, J. Freudenberger, M. Heilmaier, A. Kauffmann, Dislocation-based serrated plastic flow of high entropy alloys at cryogenic temperatures, Acta Mater. 200 (2020) 980–991, https://doi.org/10.1016/j.actamat.2020.09.052.
[58] G. Schock, Thermodynamics and thermal activation of dislocations, in: F.R. N. Nabarro (Ed.), Dislocations in Solids, North-Holland Publishing Co., Amsterdam, 1980, pp. 63–163.
[59] G.D. Liu, X.M. Luo, J.P. Zou, B. Zhang, G.P. Zhang, Effects of grain size and cryogenic temperature on the strain hardening behavior of VCoNi medium-entropy alloys, Acta Metall. Sin. (2023), https://doi.org/10.1007/s40195-023-01520-z.
[60] H. Mughrabi, Dislocation wall and cell structures and long-range internal stresses in deformed metal crystals, Acta Metall. 31 (1983) 1367–1379, https://doi.org/10.1016/0001-6160(83)90007-X.
[61] P. Hirsch, The Physics of Metals, Cambridge University Press, 2009.
[62] J.M. Park, D.C. Yang, H.-J. Kim, D.G. Kim, S. Lee, H.S. Kim, S.S. Sohn, Ultra-strong and strain-hardenable ultrafine-grained medium-entropy alloy via enhanced grain-boundary strengthening, Mater Res Lett 9 (2021) 315–321, https://doi.org/10.1080/21663831.2021.1913768.
[63] B. Gruber, I. Weißensteiner, T. Kremmer, F. Grabner, G. Falkinger, A. Schökel, F. Spieckermann, R. Schäublin, P.J. Uggowitzer, S. Pogatscher, Mechanism of low temperature deformation in aluminium alloys, Mater Sci Eng A 795 (2020) 139935, https://doi.org/10.1016/j.msea.2020.139935.
[64] D.-Y. Park, M. Niewczas, Plastic deformation of Al and AA5754 between 4.2K and 295K, Mater Sci Eng A 491 (2008) 88–102, https://doi.org/10.1016/j.msea.2008.01.065.
[65] H.R. Lin, Y.Z. Tian, S.J. Sun, Z.J. Zhang, Z.F. Zhang, Tuning the mechanical properties of copper by changing deformation temperature and recrystallization fraction, Mater Sci Eng A 853 (2022) 143734, https://doi.org/10.1016/j.msea.2022.143734.